Exp.-Nr. **A2**
Eingang:
an PAC:

Mainz Microtron MAMI

A2 Collaboration at MAMI
Spokespersons: P. Pedroni, A. Thomas

Proposal for an Experiment

"High statistics measurement of the $\omega\pi^0$ transition form factor"

Spokespersons for the Experiment :
Lena Heijkenskjöld (Institute for Nuclear Physics, JGU Mainz, Germany)
Achim Denig (Institute for Nuclear Physics, JGU Mainz, Germany)
Wolfgang Gradl (Institute for Nuclear Physics, JGU Mainz, Germany)
Sergey Prakhov (University of California Los Angeles, USA)

Abstract of Physics :
We propose to perform a new measurement of the $\omega\pi^0$ transition form factor (TFF) to explore the puzzling discrepancy between the existing experimental measurement and the numerous theoretical descriptions. Strong motivation to investigate this discrepancy comes from the close connection to the π^0 TFF, needed for the data-driven approaches aiming to improve the precision of the Standard Model calculation of the anomalous magnetic moment of the muon. The statistics of the new A2 measurement will reduce the error of the TFF slope parameter with a factor 2.8, with respect to the previous A2 measurement. Additionally, unlike previous high statistics measurements of $\omega\pi^0$ TFF from NA60, the A2 experimental setup provides an exclusive measurement with full control over background contributions. The collected data set can also be used for high statistics studies of η decays, such as the rare double radiative $\eta \to \pi^0\gamma\gamma$ decay and the $\eta \to 3\pi^0$ Dalitz plot.

Abstract of Equipment :
The experiment will be performed at the tagged photon facility of MAMI using Crystal Ball/TAPS detector setup together with particle identification detector (PID) and multi-wire proportional chambers (MWPCs).

MAMI Specifications :

beam energy	1604 MeV
beam polarization	unpolarised

Photon Beam Specifications :

tagged energy range	630 – 1492 MeV
photon beam polarization	unpolarised

Equipment Specifications :

detectors	Crystal Ball/TAPS, PID, MWPCs
target	liquid hydrogen

Beam Time Request :

set-up/test with beam	48 hours
data taking	850 hours

List of participating authors:

- **Institut für Physik, University of Basel, Switzerland**
  D. Ghosal, N. Jermann, B. Krusche, A. Kaeser, C. Meier
- **Institut für Experimentalphysik, University of Bochum, Germany**
  G. Reicherz
- **Helmholtz–Institut für Strahlen- und Kernphysik, University of Bonn, Germany**
  F. Afzal, R. Beck, A. Thiel, Y. Wunderlich
- **JINR, Dubna, Russia**
  N.S. Borisov, I. Gorodnov, A. Lazarev, A. Neganov, Yu.A. Usov
- **SUPA School of Physics and Astronomy, University of Glasgow, UK**
  S. Gardner, K. Livingston, I.J.D. MacGregor
- **Racah Institute of Physics, Hebrew University of Jerusalem, Israel**
  G. Ron
- **Kent State University, Kent, USA**
  D.M. Manley
- **Institut für Kernphysik, University of Mainz, Germany**
  P. Achenbach, M. Biroth, F. Cividini, A. Denig, P. Drexler, M.I. Ferretti-Bondy, W. Gradl, L. Heijkenskjöld, V.L Kashevarov, P.P. Martel, E. Mornacchi, M. Ostrick, V. Sokhoyan, C. Sfienti, M. Thiel, A. Thomas, S. Wagner, J. Wettig
- **University of Massachusetts, Amherst, USA**
  R.Miskimen
- **Institute for Nuclear Research, Moscow, Russia**
  G. Gurevic
- **INFN Sezione di Pavia, Pavia, Italy**
  A. Braghieri, S. Costanza, P. Pedroni
- **Department of Physics, University of Regina, Canada**
  G.M. Huber
- **Mount Allison University, Sackville, Canada**
  D. Hornidge
- **George Washington University, Washington, USA**
  W.J. Briscoe, E.J. Downie, I.I. Strakovsky
- **Department of Physics, University of York, UK**
  M. Bashkanov, D.P. Watts, D. Werthmüller
- **Rudjer Boskovic Institute, Zagreb, Croatia**
  M. Korolija

1 Introduction

The electromagnetic meson transition form factor (TFF) describes the interaction between mesons and photons. It is needed in order to explain the difference between the point-like interaction given by Quantum Electrodynamic (QED) calculations and the experimental results. Therefore, to study TFFs is to probe the electromagnetic structure of the mesons. TFFs display a dependence on the transferred momentum of the involved photons, q^2, both in the space-like and the time-like region. However, only certain q^2-regions are experimentally accessible. The interaction of $\omega - \pi^0 - \gamma^*$ can be studied in either the reaction $e^+e^- \to \gamma^* \to \omega\pi^0$ or the decay $\omega \to \pi^0\gamma^* \to \pi^0\ell^-\ell^+$, where $\ell = e/\mu$. The latter allows to study the TFF in a q^2-region where $4m_\ell^2 \leq q^2 \leq (m_\omega - m_{\pi^0})^2$. The former is limited to q^2 above the $\omega\pi^0$ production threshold.

This proposal focuses on the investigation of the ω decay, where the TFF relates to the decay width [1],

$$\frac{d\Gamma(\omega \to \pi^0\ell^+\ell^-)}{dq^2\Gamma(\omega \to \pi^0\gamma)} = [QED]\left|F_{\omega\pi^0}(q^2)\right|^2. \tag{1}$$

The left hand side of Eq. (1) shows the experimentally accessible differential decay rate. By convention, the decay process resulting in a real photon, rather than the dileption, is used for normalisation. The right hand side of Eq. (1) is given by a term calculable from QED and the modulus squared of $\omega\pi^0$ TFF. To facilitate comparison between different results, the $F_{\omega\pi^0}(q^2)$ can be parametrised using a one-pole approximation where the slope at $q^2 = 0$ is given by Λ^{-2},

$$F_{\omega\pi^0}(q^2) = \frac{1}{1 - q^2\Lambda^{-2}} \quad \text{and} \quad \Lambda^{-2} = \left.\frac{dF_{\omega\pi^0}(q^2)}{dq^2}\right|_{q^2=0}. \tag{2}$$

1.1 Theoretical predictions

For calculations involving light mesons, the strong coupling constant becomes too large to allow precision results using perturbative Quantum Chromodynamic (QCD) calculations. Instead, several non perturbative approaches, such as phenomenological models and Lattice QCD, as well as effective field theories have been developed. One of the most famous models is Vector Meson Dominance (VMD) that originated in the Theory of Strong Interactions proposed by J. J. Sakurai [2]. VMD was developed before QCD and uses the light vector mesons to explain the interaction between hadrons and photons. Another well established approach, which incorporates the symmetries of QCD, is Chiral Perturbation Theory (ChPT). ChPT allows for precise calculations of properties and interactions involving the light pseudoscalar mesons, which are identified as the Goldstone bosons. To include the vector mesons, one approach was made by constructing a chiral Lagrangian which besides the Goldstone bosons also includes the nonet of light vector mesons. A set of counting rules was proposed within this approach, where the relevant parameters are determined from comparisons to known processes [3]. This allows for predictions of e.g. $\omega \to \pi^0\ell^-\ell^+$.

The interaction of interest here has also been considered using dispersion theory. In Ref. [4], the dispersion relation for the $V \to \pi^0\gamma^*$ decay, where $V = \omega/\phi$, is set up by considering $\pi\pi$ as the intermediate state. This allows to express the $V\pi^0$ TFF using only the $\pi\pi$ phase shift and the $V \to 3\pi$ partial-wave amplitude. The latter was calculated in

a previous publication [5]. To account for inelastic contributions, a subtraction constant is introduced, which was fixed to reproduce the $V \to \pi^0\gamma$ partial width. In Ref. [6], a similar approach is taken where the dispersion relation for the $V\pi^0$ TFF is set up using the pion vector form factor and the $V \to 3\pi$ decay amplitude, which was calculated in the same paper. The main difference to the previous approach is the method for dealing with the inelastic contributions. In Ref. [6], the dispersive integral is split into an elastic and inelastic part where the latter is parametrised. Unlike the previous approach, this takes into account the change in the analytical properties of the $V\pi^0$ TFF induced by the opening of inelastic channels. For the $V \to 3\pi$ decay amplitude, only one parameter is used and it is fixed to reproduce the measured $V \to 3\pi$ decay width. For the $V \to \pi^0\gamma^*$ form factor, only the first parameter is given by the real-photon decay width. Additionally, a second and a third parameter are given by fits to the experimental data of the $\omega\pi^0$ TFF from Ref. [7].

In Ref. [8], the issue with how the $\omega\pi^0$ TFF is affected by the contributions in the inelastic region is addressed by using a formalism of unitarity bounds. This allows them to set up an integral condition on the form factor over the inelastic region, derived from unitarity and perturbative QCD. Implementing this into the dispersion relation given by Ref. [4] produces upper and lower limits on the $\omega\pi^0$ TFF in the decay region.

The approachs presented in Ref. [9] builds on the procedure developed in Ref. [8]. Instead of using a theoretical inequality to constrain the TFF in the inelastic region, now the data provided by CMD-2 [10] for the $e^+e^- \to \omega\pi^0$ was used. Similar as in Ref. [8], known dispersion relations were used to express the $\omega\pi^0$ TFF in the decay region. The modulus of the TFF in the inelastic region was obtained as an interpolation of the experimental data points and continued as a smooth $1/t$-decrease. From this, a much more stringent bound on the modulus of the TFF in the decay region could be extracted.

1.2 Previous experimental measurements

The first experimental measurement of the $\omega\pi^0$ TFF was done using data collected by the Lepton-G experiment [11]. The ω mesons are produced in the $\pi^-p \to \omega n$ reaction and detected via the $\omega \to \pi^0\mu^+\mu^-$ channel. The photons from the π^0 decay are fully reconstructed using 64 lead-glass counters. The muons are detected in a magnetic spectrometer with proportional and wire spark chambers. The resulting 60 ± 9 signal events are used to produce an $\omega\pi^0$ TFF distribution. When it is compared to a VMD-prediction, a clear discrepancy between theory and experiment is visible.

The NA60 experiment at the CERN SPS has published two high statistics results on the $\omega\pi^0$ TFF. In the first one, peripheral In-In collisions at 158 GeV/nucleon are used as production method [7]. In the second one, p-A collisions are exploited. The 9 different nuclear targets (A = Be, Cu, In, W, Pb and U) are all simultaneously exposed to the incident 400 GeV proton beam [12]. The thicknesses of the different targets were set to assure similar statistics from all samples. In both analyses, only the muon pairs are reconstructed. A Monte Carlo cocktail consisting of $\eta \to \mu^+\mu^-\gamma$, $\eta \to \mu^+\mu^-$, $\omega \to \mu^+\mu^-\pi^0$, $\omega \to \mu^+\mu^-$, $\eta' \to \mu^+\mu^-\gamma$, $\rho \to \mu^+\mu^-$, $D\bar{D}$, and $\phi \to \mu^+\mu^-$ is fitted to the uncorrected data distribution to extract the normalisations of the various contributions, see Fig. 1a. All signals except $\eta \to \mu^+\mu^-\gamma$, $\omega \to \mu^+\mu^-\pi^0$ and $\rho \to \mu^+\mu^-$ are subtracted and the resulting distribution is corrected for acceptance, shown in Fig. 1b. A fit is performed using a sum of theoretical descriptions of the three remaining signals. The two

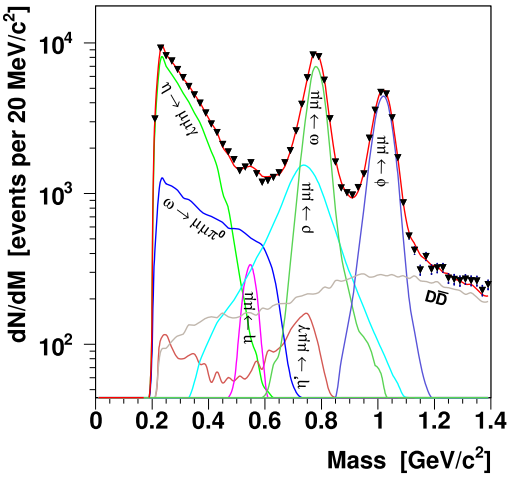

(a) Target-integrated mass spectrum compared to the MC hadron cocktail.

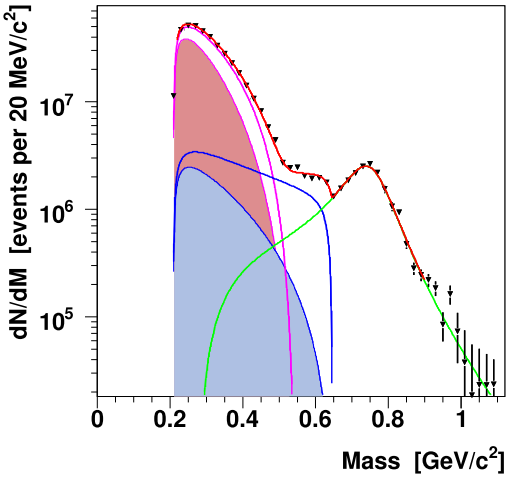

(b) Acceptance- and efficiency-corrected mass spectrum after MC subtraction.

Figure 1: The measured $\mu^+\mu^-$ mass spectra from NA60 [12]. (a): The mass spectrum is compared to all contributions to the MC hadron cocktail after all scaling parameters have been extracted from fit to data. (b) Corrected mass spectrum after subtracting all MC except $\eta \to \mu^+\mu^-\gamma$ (pink line), $\omega \to \mu^+\mu^-\pi^0$ (blue line) and $\rho \to \mu^+\mu^-$ (green line). Shaded areas are QED expectations.

Dalitz decays were described in a similar fashion as given in Eq. (1) with the form factors being parametrised as in Eq. (2). For the ρ decay, a line shape, including a Boltzmann term, characteristic for hadroproduction of the ρ meson is used. This fit provides the slope parameters of the η and $\omega\pi^0$ TFFs and also allows to disentangle the three contributions and plot the separate TFF distributions.

1.3 Motivation

As can be seen in Fig. 2, there is a clear discrepancy between the numerous theoretical predictions and the experimental results from NA60 and Lepton-G. This has been a strong motivator for the efforts from theory side to improve the description of the $\omega\pi^0$ TFF in the q^2-region covered by the decay. Section 1.1 above briefly describes the various ways the theoretical models incorporates the contributions from the inelastic region to the dispersion integral. It is interesting to note that even the rather loose bound from Ref. [8] misses the last data points in the high q^2 region. This can be interpreted as a suggestion that these $\omega\pi^0$ TFF data points violate even very general unitarity bounds. A debatable source of the discrepancy between the very precise NA60 results and theory, concerns the method of NA60 for dealing with the irreducible backgrounds listed in Sec. 1.2. As seen in Fig. 1a, the high mass region of the $\omega \to \mu^+\mu^-\pi^0$ distribution is populated by several of the irreducible background contributions, which are subsequently subtracted using the coherently added hadronic decay cocktail.

The conflict between the detailed theoretical predictions and the high statistics results from NA60 clearly demands a complementary high statistics study using a setup utilising an exclusive reconstruction and analysis approach with a complete control of the

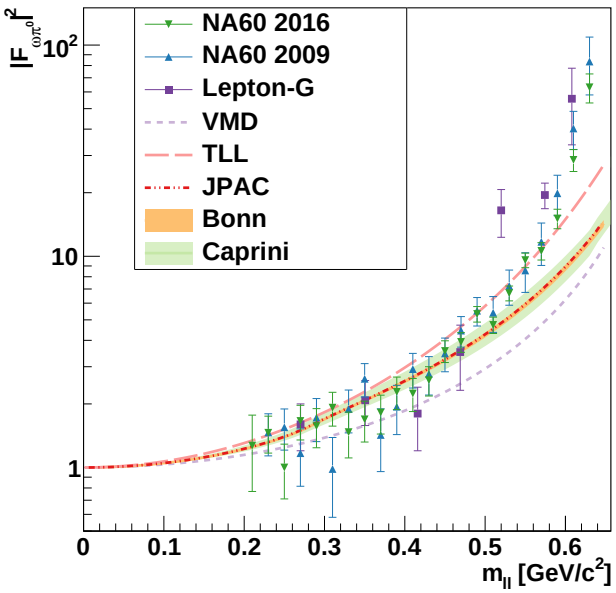

Figure 2: The $\omega\pi^0$ TFF distribution in the $q^2 = m^2_{\ell\ell}$-region covered by the $\omega \to \pi^0\ell\ell$ decay. All experimental results mentioned in Sec. 1.2 are shown. The theory predictions from VMD and the chiral Lagrangian approach (labelled TLL) are given by Ref. [3]. The dispersive analysis result from Ref. [4] (Bonn) shown here, with error borders, includes the full $V \to 3\pi$ rescattering. The plotted dispersive analysis result from Ref. [6] (JPAC) is where only one parameter is used for the inelastic region. The dispersive analysis from Ref. [9] (Caprini) shown here is uses the $V \to 3\pi$ partial-wave amplitude given by Ref. [4].

background. The A2 experiment, studying the $\omega \to e^+e^-\pi^0$ channel, provides a excellent option as it allows for a full reconstruction of all final state particles as well as a complete knowledge of the initial state when using photo-induced reactions on protons. Additionally, the e^+e^- final state allows to reach much lower q^2 values than the $\mu^+\mu^-$ final state which provides a more certain determination of the $\omega\pi^0$ TFF slope, Λ^{-2}.

To emphasize the need to resolve this theory-data discrepancy, it is relevant to point out that the $\omega\pi^0$ TFF is related to the doubly virtual π^0 TFF when one of the virtual photons couples to an ω meson. Furthermore, light pseudoscalar meson TFFs play a significant role in the efforts of increasing the precision of the Standard Model (SM) calculations of the anomalous magnetic moment of the muon, a_μ. Currently, there is a $3-4\sigma$ discrepancy between the experimentally measured value of a_μ [13] and the SM prediction [14]. With ongoing efforts to further reduce the experimental uncertainty [15, 16], efforts are also made on theory side to reduce the a_μ^{SM} uncertainty. If the discrepancy is found to reach even higher significance, it would be a clear indication of physics beyond the SM. The largest contribution to the a_μ^{SM} uncertainty comes from the strong sector, from hadronic vacuum polarisation and hadronic Light-by-Light (LbL) scattering. The latter is illustrated in Fig. 3 along with the meson pole diagram where light pseudoscalar mesons, $P = \pi^0,\ \eta,\ \eta'$, give the largest individual contribution to the a_μ^{LbL} uncertainty. The amplitude of the coupling between the light meson and the two virtual photons is directly given by the P TFF. Hence, the data-driven theory approaches, developed to reduce the a_μ^{LbL} uncertainty, need input from experimental measurements of, among

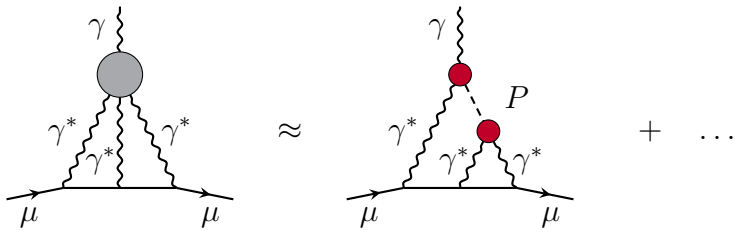

Figure 3: Illustration of the hadronic Light-by-Light scattering term contributing to the SM calculation of a_μ. One of the terms contributing to the LbL scattering is the meson pole diagram where the $P - \gamma^* - \gamma^*$ interactions are marked as red circles.

others, TFFs of pseudoscalar mesons [17]. Due to the $\omega\pi^0$ being a special case of doubly virtual π^0 TFF, any theory aiming to fully describe the latter should also accurately describe the former.

2 Measurements at the A2 experiment

2.1 Completed $\omega\pi^0$ TFF measurement at A2

A2 has completed an analysis of the $\omega\pi^0$ TFF based on data collected in beam times during 2007 and 2009. The result was published in 2017 [18]. The conditions used for data collection and the analysis procedures will be outlined here in order to motivate the suitability of the A2 experiment as well as illustrate the improvements reachable with a new A2 measurement. The conditions for the two different data taking campaigns are outlined in Tab. 1. As seen, MAMI-C energies were used in both campaigns, as well as an amorphous radiator providing an unpolarised photon beam tagged up to E_γ^{max}. The trigger conditions are primarily relying on the online summation of the energy deposition in the Crystal Ball detector, see Sec. B.1. In addition, a multiplicity trigger was used (M2+ or M3+). In this trigger, hardware clusters were defined by a block of 16 adjacent crystals and the trigger conditions were fulfilled if a given number (2 or 3) of the clusters contained at least 1 crystal with an energy deposit larger than 30 MeV. The data collection time during 2007 was nearly twice as long as in 2009. However, due to differences in the run conditions (such as trigger settings and target length), the event rate of the signal is lower in 2007 than in 2009. In the end, the two campaigns yielded similarly sized samples of $\omega \to \pi^0 e^+ e^-$ events, $N_{\pi ee}^{2007} = 610$ and $N_{\pi ee}^{2009} = 460$.

Table 1: The conditions used for data collection during 2007 and 2009. For clarifications of the conditions, see text.

	2007	2009
E_{e^-}	1508 MeV	1557 MeV
E_γ^{max}	1402 MeV	1448 MeV
Radiator	10 μm Cu	10 μm Cu
Collimator	4 mm	4 mm
Target	5 cm LH2	10 cm LH2
Trigger	$E_{CB}^{sum} > 320$ MeV and M2+	$E_{CB}^{sum} > 340$ MeV and M3+

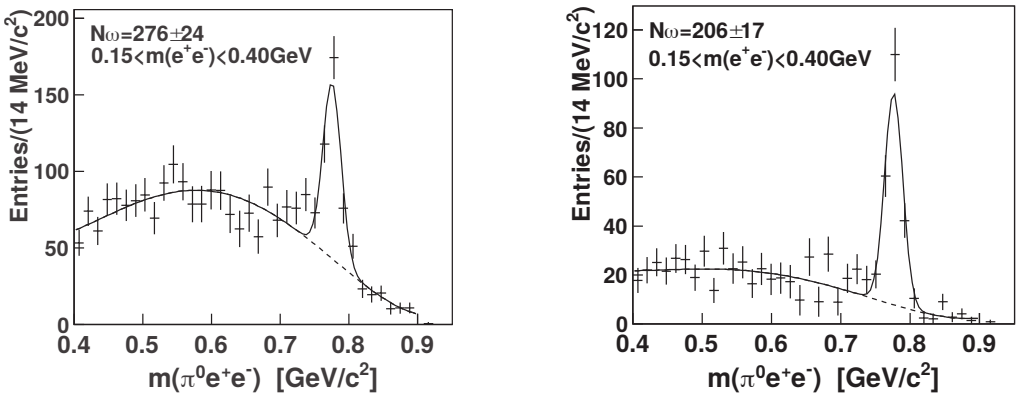

(a) (b) .

Figure 4: The $m_{\pi ee}$ distributions obtained in the m_{ee} range 150-400 MeV from data collected in 2007. (a) After tight cuts on CB-cluster shower shapes and (b) after additional cuts on dE/dx in the PID.

To select the $\omega \to \pi^0 e^+ e^-$ events in the offline analysis, exactly 5 reconstructed clusters are required. Further event identification is done using a constrained kinematic fit of the reconstructed particles. The constraint consists of a requirement of conservation of energy and momentum assuming the reaction $\gamma p \to 4\gamma p$. For simplicity, and due to their low mass, the leptons are treated as photons in the kinematic fit constraint. Photons and leptons are further identified by correlating the clusters in CB to hits in the PID detector. The dominant $\omega \to \pi^0 \gamma$ decay channel can mimic the Dalitz decay via a conversion of one of the photons into an e^+e^- pair. This resonant background contribution is suppressed by requiring the electron and positron to be measured in different PID elements. Cuts on dE/dx in PID are also used to suppress dominant non resonant background from $\gamma p \to \pi^0\pi^0$ and $\gamma p \to \eta\pi^0$. The second most dominant decay channel, $\omega \to \pi^+\pi^-\pi^0$, also contributes to the background. This contribution is reduced by applying cuts on the CB-cluster shower shapes, such as number of crystals per cluster vs cluster energy or the effective cluster radius vs cluster energy. Figure 4 shows the impact of the dE/dx cuts and also the clean separation between the $\omega \to \pi^0 e^+ e^-$ signal and the background achievable using the A2 setup.

The events remaining after signal selection are sorted into m_{ee}-bins. For each bin, the ω-peak content in the corresponding $m_{ee\pi}$ distribution is extracted and efficiency corrected. As seen in Eq. (1), the $|F_{\omega\pi}(q^2)|^2$ distribution is obtained by dividing out the $[QED]$ term and the total number of $\omega \to \pi^0\gamma$ events produced. Figure 5 is showing the resulting $\omega\pi^0$ TFF distribution and how it compares to the data points from NA60 and Lepton-G as well as the available theoretical predictions. The error bars on the A2 data points are the squared sum of statistic and systematic errors. As can be seen, the error bars on the A2 result does not provide a convincing separation between the previous experimental results and the theoretical predictions. But the nominal values of each data point are systematically lower than the NA60 results and more in agreement with the theoretical models.

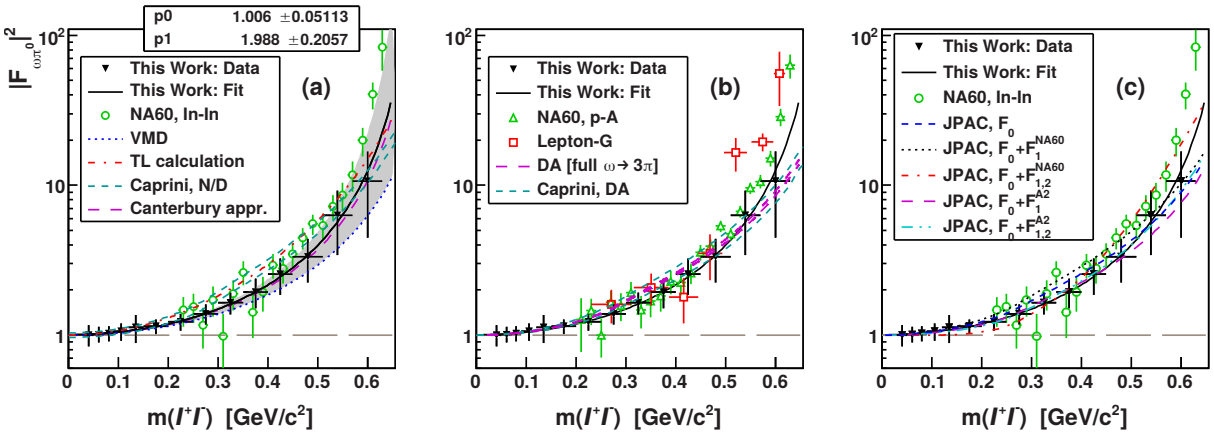

Figure 5: The figure is taken from Ref. [18] and is showing the published A2 results, labelled as This Work, and how it compares to the other available experimental results as well as theoretical predictions.

2.2 A2 upgrades

During 2013-2014, the A2 data acquisition system was substantially upgraded. The data throughput was increased due to upgrades of the read-out electronics. Moreover, by automating the initialisation and coupling of the readout systems of the separate detectors, the time needed to restart the data acquisition was reduced from $\sim$ 10 minutes to 5 seconds. Overall, the upgrades performed was estimated to double the speed of effective data taking [19].

During 2017-2018 the photon tagger was completely upgraded, restoring many broken and inefficient channels. Furthermore, with the new tagger geometry, the neighbouring detector elements are no longer overlapping. Hence, instead of the coincidence condition of two neighbouring elements which was used before, the new setup reads out each detector element separately. This, along with the instalment of fast SiPMT for each element, allow an increase in the rate at which the individual counters are able to operate, from $\sim$ 1 MHz up to 2.5 MHz.

Altogether, the upgrades resulted in an experiment system allowing for high statistic data taking. This has been proven in the data taking campaigns following the tagger upgrade. For instance, two beam times during 2018 was dedicated to a high statistics measurement of the π^0 TFF. They can be compared to a previous study done by A2 using data collected during 2008 and 2013. Direct comparisons are ambiguous due to different run conditions. However, the conditions for the 2008 and 2018 data sets are similar enough to be used as an estimate for the data rate improvement. One main difference was the trigger conditions, since in 2008 the threshold on the CB energy sum was 40 MeV lower and a multiplicity trigger, M2+, was used. Another main difference was the position of the polarisation peak in the photon beam energy distribution, see Fig. 10. In 2018, this was optimally placed in the $\Delta(1232)$ resonance region in order to increase the dominant π^0 production channel. One figure of merit is the signal event rate, i.e. the ratio of $\pi^0 \to e^-e^+\gamma$ events collected and the time spent on data collection. From the completed analysis of the 2008 data, this rate amounted to an average of 445 events/hour. From a preliminary analysis of the 2018 data, this rate was 2550 events/hour. Hence a rate increase of 5.5 was achieved. Another figure of merit, which better reflects the data

Table 2: The run conditions for the 2019 beam times.

	2019
E_{e^-}	1604 MeV
E_γ^{max}	1492 MeV
Radiator	10μm Fe/Co alloy
Collimator	3 mm
Target	10 cm LH2
Trigger	$E_{CB}^{sum} > 450$ MeV

acquisition improvements, is the trigger rate achieved during the two separate beam times. In 2008, the trigger rate during data collection was 780 Hz while in 2018 the trigger rate was on average 3500 Hz. This corresponds to a 4.5 times increase. As demonstrated, the upgrades to the A2 experimental setup resulted in a significant increase in data collection rate.

2.3 Feasibility from collected data

During the second half of 2019, two beam times were dedicated to producing η and ω mesons, allowing to both test the proposed conditions for the $\omega\pi^0$ TFF measurement as well as estimate the achievable rates. Table 2 shows the conditions used during these beam times. As seen in Fig. 6, the ω photoproduction cross section is largely invariant at higher beam energies. Hence, a larger E_γ-coverage by the tagger would increase the produced ω yield. By running at maximum MAMI-C energy, E_{e^-}=1604 MeV, the tagger covers a E_γ region up to 50 MeV above the η' production threshold. The first 96 tagger elements, up to $E_\gamma = 633MeV$, was turned off to reduce the contribution from the low energy region of the bremsstrahlung spectrum. The threshold of the summed energy deposit in CB, used as the trigger condition, was chosen to maximally suppress the contributions from single and double neutral pion production while still triggering on η production events.

A preliminary analysis has been performed on the collected data. A decent analysis of the $\omega \to \pi^0 e^+ e^-$ channel requires a well tuned calibration and refined analysis cuts. Therefore, a more stable estimate of the increase in signal rate can be done by focusing

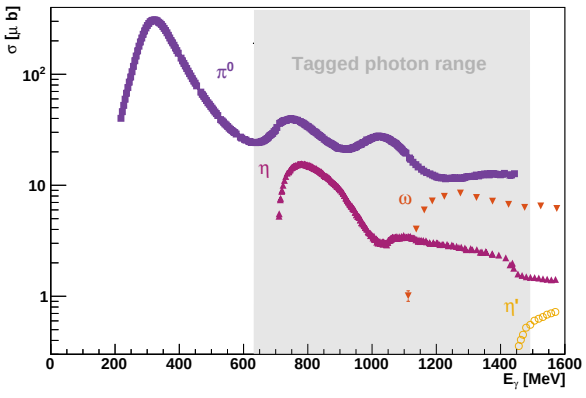

Figure 6: The cross sections for the photo production of the lighter mesons and the tagged photon energy range during the 2019 beam times.

on a simple selection of the more probable decay channel $\omega \to \pi^0\gamma$. This has been done by applying the same selection on both the older data and the newly collected one. The 3+ multiplicity trigger, used in the 2009 data collection, affects the $\omega \to \pi^0\gamma$ more than the 2+ multiplicity trigger used in 2007. Therefore a comparison was done between the full data set collected in 2007 and a selected data set from 2019 for the $\omega \to \pi^0\gamma$ channel. Using the number of $\omega \to \pi^0\gamma$ events found in these analyses, $N_{\pi\gamma}^{2007} = 310678(679)$ and $N_{\pi\gamma}^{2019} = 473307(1098)$, and the fact that 610 $\omega \to \pi^0 e^+e^-$ events were collected in the 2007 data set, one can estimate the amount of $\omega \to \pi^0 e^+e^-$ events in the selected data set from 2019 data to be $\left(N_{\pi ee}^{2007} \times N_{\pi\gamma}^{2019}\right) \ / \ N_{\pi\gamma}^{2007} = 930(3)$. The sum of the length of all the runs in the selected data set from 2019 is 107 hours which gives an event rate of **8.7 events/hour**. This rate will be used to estimate the beam time needed to reach a competitive statistics in a new measurement. The full time it took to collect the selected data set from 2019 is 180 hours. This includes breaks in data collection due to tagging efficiency measurements and repairs of our experiment setup or MAMI. The event rate including these breaks is 5.2 events/hour.

Another interesting result from this feasibility study is to compare the increase in rate of $\omega \to \pi^0 e^+e^-$ events in 2019 data set (including breaks) to the older data set. For this comparison it is better to use the rate in 2009 data, since the conditions are a bit more similar to 2019 beam times. E.g. the length of the target is the same and the beam energy used in 2009 was higher than in 2007. With a yield of 460 $\omega \to \pi^0 e^+e^-$ events and a data collection time of 382 hours (including breaks) the rate was, on average, 1.21 events/hour in 2009. This is nearly 4.3 times lower than the event rate of 5.2 events/hour estimated for 2019, which is in agreement with the observations of improvements in data collection rate made in Sec. 2.2.

3 Expected precision and beam time estimate

As outlined in Sec. 1.3, the purpose of this measurement is to achieve a high statics measurement of the $\omega\pi^0$ TFF. This is greatly needed in order to investigate the discrepancy observed between the theoretical predictions and the existing experimental measurements. Hence, the aim is to reduce the uncertainty of the data points from the previous A2 measurement. Assuming the systematic error remains unchanged, which was reported as an average of 20% of the statistical errors in previous A2 measurement, one can calculate the effect an increase in statistics would have on the error bars from previous A2 result. As seen in Fig. 7a, an increase of a factor 9 yields a near 1 σ separation between the existing data points in the highest $m_{\ell\ell}$ bin. Hence, this presents a reasonable choice for the size of the new data sample. The error of the slope parameter, Λ^{-2}, can be extracted by fitting the $\omega\pi^0$ TFF parametrisation given in Eq. (2) to data points with the reduced errors. As seen in Fig. 7b, the chosen factor of 9 increase in statistics provides a competitive error size for a new value of the slope parameter. Assuming that the central value of the A2 slope parameter remains unchanged, the projected accuracy of the new A2 measurement will increase the discrepancy between the current PDG value of Λ^{-2} for $\omega \to \mu^+\mu^-\pi^0$ and the A2 result from 1.1 σ to 2.8 σ.

Using a rate of $\omega \to \pi^0 e^+e^- = 8.7$ events/hour, as estimated in Sec. 2.3, and aiming to collect 9×1070 events, one would need 1100 hours of data collection. During the test beam times in 2019, 350 hours of good data were collected which can be used for this

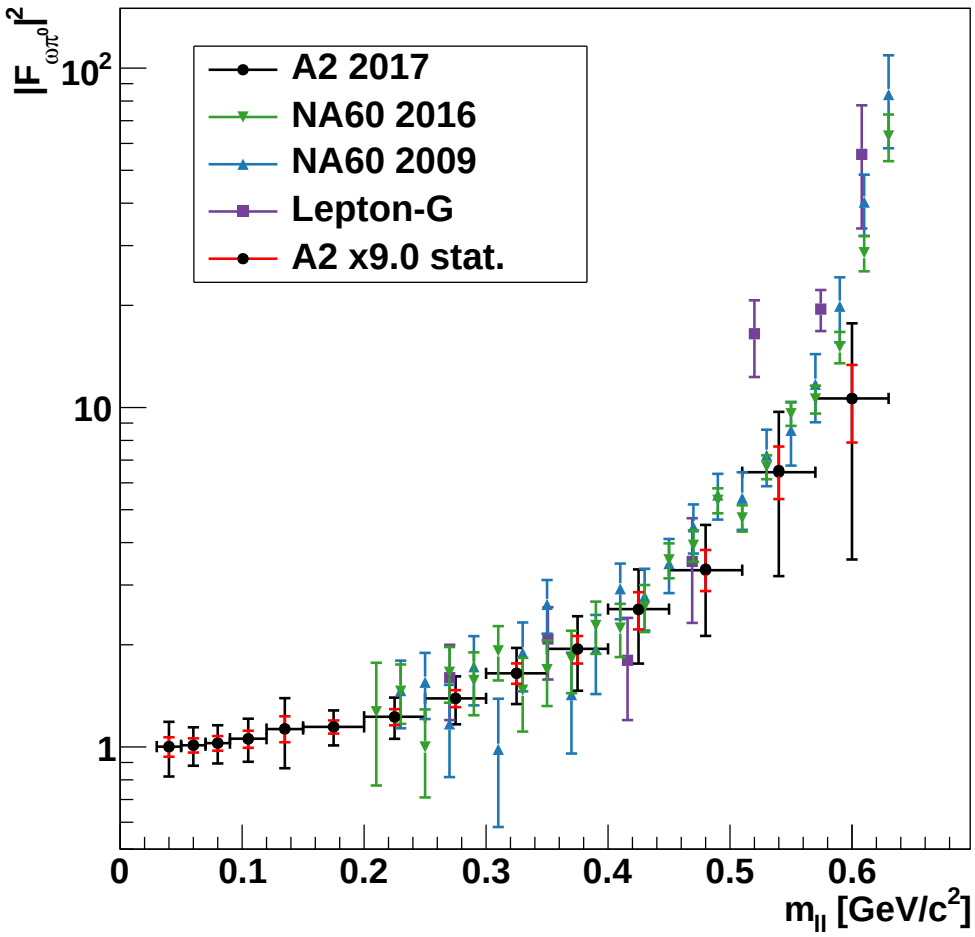

(a) Experimental values of the $\omega\pi^0$ TFF with existing and projected error bars.

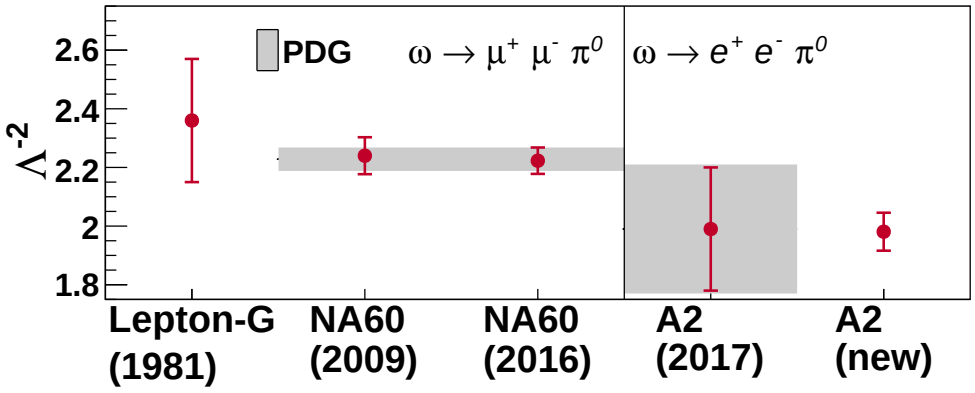

(b) Slope parameters of $\omega\pi^0$ TFF.

Figure 7: (a) The measured $\omega\pi^0$ TFF values as given by Lepton-G, NA60 and A2. The red error bars on top of the A2 data points show the projected precision achieved if the statistic sample would be increased by a factor of 9. (b) The slope parameters for each experiment along with the projected error for a new measurement.

study and hence only 750 hours more are needed. During 2019, 36 hours of good data with an empty target were collected. This was deemed enough to investigate possible contribution from the target cell. Additional 11 hours were spent on tagging efficiency measurements. Scaling these numbers to match the remaining 750 hours to be collected, gives that an additional 77 hours are needed for empty target data collection and 24 hours are needed for tagging efficiency measurements. In total, the requested beam time to achieve the proposed data sample size is **850 hours**.

Based on the 2019 beam times, an estimation of the time needed including planned and unplanned breaks in data taking, can be extracted from the signal rate of 5.2 events/hour. As mentioned in Sec. 2.3, this rate also includes the time spent on performing tagging efficiency measurements and hence only time needed for more data taking with empty target should be added. Scaling up the 750 hours needed for pure data collection and adding the 77 hours proposed for empty target data taking results in approximately seven to eight weeks of beam time.

4 Further uses of new high statistics data sample

Several competitive publications from the A2 collaboration has been made using the 2007 + 2009 data sets. The high statistics measurement proposed here would then provide a great improvement for these studies, as well as others focusing on the η and ω mesons. This section will highlight two such η decay studies. As the η cross section peaks towards the treshold region, see Fig. 6, the increase in η yield in the new data set will not be as high as the projected increase of ω yield. Preliminary analysis of the 2019 and the 2007 data sets indicates that the η yield is $\sim 30\%$ lower than the ω yield.

4.1 The rare $\eta \to \pi^0\gamma\gamma$ decay

In 2014, the A2 collaboration published the so far most precise measurement of the $d\Gamma(\eta \to \pi^0\gamma\gamma)/dm^2(\gamma\gamma)$ distribution and an extracted value of the decay width $\Gamma(\eta \to \pi^0\gamma\gamma)$ [22].

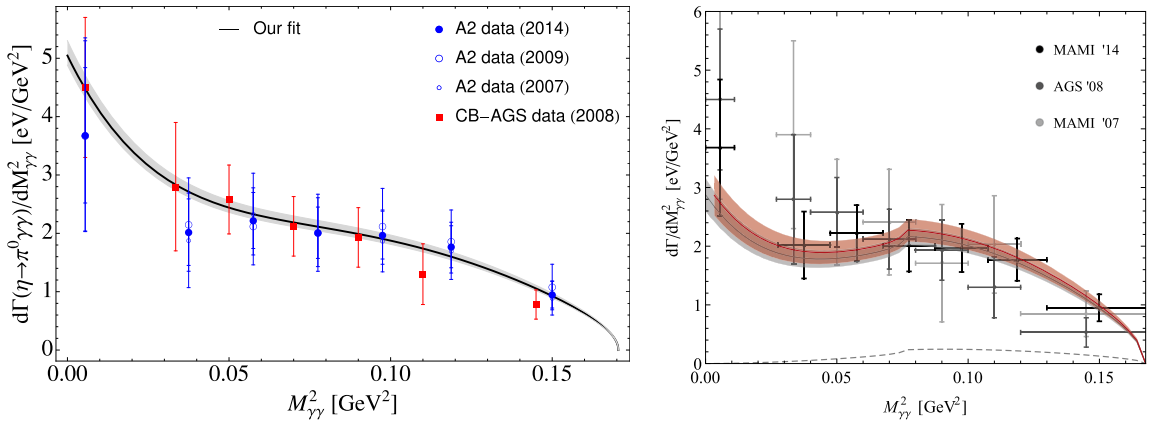

(a) From Ref. [20] (b) From Ref. [21]

Figure 8: The $m^2(\gamma\gamma)$ dependence of the decay width as calculated in Ref. [20] and Ref. [21] and how it compares to data from the A2-MAMI collaboration (2014, 2009, 2007) and the Crystal Ball Collaboration at the AGS.

This result uses 1.2×10^3 $\eta \to \pi^0\gamma\gamma$ events from the 2007 and 2009 data sets discussed in this proposal.

This rare doubly radiative decay is of great interest since it probes higher order terms of ChPT, the major contribution coming from $\mathcal{O}(6)$ [23]. Recently it has also been used to benchmark calculations using Linear Sigma Model and Vector Meson Dominance [20] as well as dispersion formalism [21]. The former aims for a good description of the $\eta' \to \pi^0\gamma\gamma$ and $\eta' \to \eta\gamma\gamma$ decays. The latter means to describe the $\gamma\gamma \to \pi^0\eta$ reaction as it provides information on the $a_0(980)$ and $a_2(1320)$ resonances. Figure 8 shows the result from these two calculations compared to the experimental data from A2 and how they both would benefit from a more precise measurement of $d\Gamma(\eta \to \pi^0\gamma\gamma)/dm^2(\gamma\gamma)$.

4.2 Dalitz plot study of $\eta \to \pi^0\pi^0\pi^0$

The A2 collaboration has published several measurements of the $\eta \to \pi^0\pi^0\pi^0$ Dalitz plot. The most recent [24], containing 7×10^6 events, is based on the 2007 and 2009 data set discussed in this proposal. Studies of the $\eta \to 3\pi$ Dalitz plot has been used to determine the quark mass ratio $Q^2 = (m_s^2 - m_{ud}^2)/(m_d^2 - m_u^2)$. In Ref. [25] such an extraction is done using dispersive analysis where the subtraction constants needed are obtained from fits to an experimental $\eta \to \pi^+\pi^-\pi^0$ Dalitz plot distribution [26]. The density distribution from the neutral channel, provided by A2, allows a strong test of the theory prediction, as seen in Fig. 9. The additional interest of the neutral channel consist of the predicted cusp at the $\pi^+\pi^-$ threshold. Using a non-relativistic effective field theory (NREFT) framework this effect has been predicted to be of 1% magnitude [27], see Fig. 9b. The published A2 result yields the currently most precise measurement of the parametrisation of the Dalitz plot density distribution as well as a first indication of the cups effect. However, as the cusp effect is currently only indicated from fits of parametrisations, an even larger data set would strengthen the observation of the cusp as well as the non-linearity of the parametrisation of the $\eta \to \pi^0\pi^0\pi^0$ Dalitz plot density distribution.

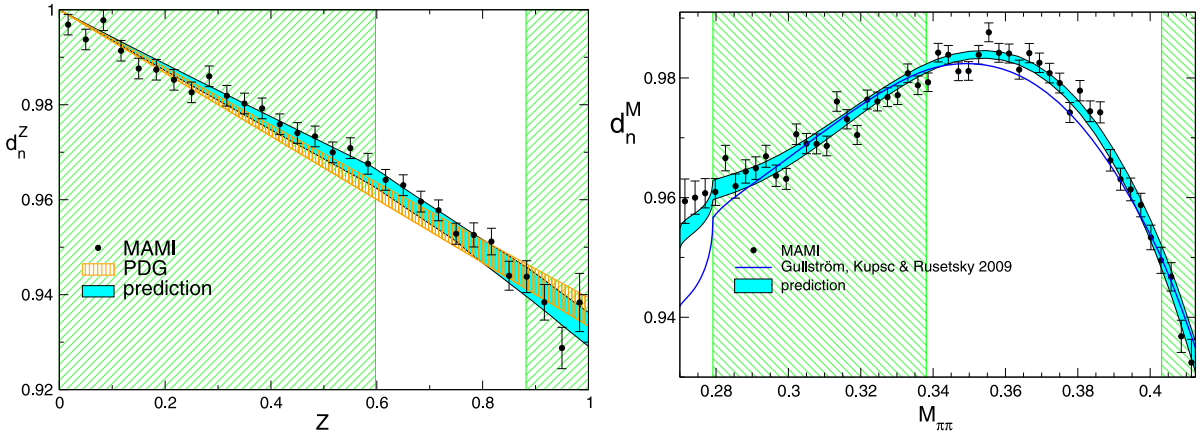

(a) $Z \equiv$ Dalitz plot radial coordinate

(b) $M_{\pi\pi} = \sqrt{s}$ (GeV units)

Figure 9: From Ref. [25]. Comparison of $\eta \to 3\pi^0$ Dalitz plot density distributions from the most recent study by A2 [24] and the prediction made by the dispersive analysis in Ref. [25].

A Experimental apparatus

A.1 Photon Beam

The A2 photon beam is derived from the production of Bremsstrahlung photons during the passage of the MAMI electron beam through a thin radiator. Using an amorphous radiator produces an unpolarised beam. However, the resulting photons can also be circularly polarised, with the application of a polarised electron beam, or linearly polarised, in the case of a crystalline radiator. The degree of polarisation achieved is dependent on the energy of the incident electron beam (E_0), the energy range of interest, and in the case of linear polarisation on the photon collimator size. Together, these currently result in a peak of ∼75% for linear polarisation (Fig. 10a) and ∼85% for circular polarisation (Fig. 10b). The collimator size, as well as the electron beam energy, also affect the ratio of photons that reach the target to those produced in the Bremsstrahlung process. Typical values for this ratio, denoted as the tagging efficiency, are shown in Tab. 3. The upgraded A2 Photon Tagger (Fig. 11) provides energy tagging of the photons by detecting the post-radiating electrons with a single-counter time resolution $\sigma_t = 0.1$ ns [28]. With the upgrade, individual counters can now operate reliably above 1 MHz, although the loss due to pile-up is ∼1.8% per 1 MHz rate. A typical limit of 2.5 MHz is employed to keep the pile-up loss below 5%. Photons can be tagged in the momentum range from 4.3 to 93.0% of E_0, with resolutions varying from 0.4 to 0.05% of E_0, respectively. This relationship, along with sample rate distributions, is shown in Fig. 12.

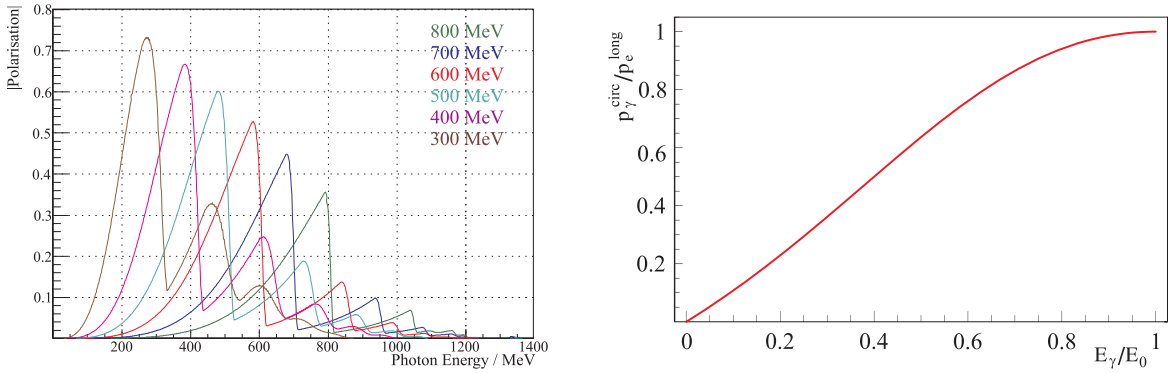

(a) Linear polarisation

(b) Helicity transfer

Figure 10: (a) Linear polarisation available with the current collimation system for a variety of crystal orientations. (b) Helicity transfer from the electron to the photon beam as function of the energy transfer. The MAMI beam polarisation is $P_e \approx 85\%$.

Table 3: Tagging efficiencies, in %, for typical incoming electron beam energies (E_0) and photon collimator diameters (d_{col}).

E_0 (↓) / d_{col} (→)	1.5 mm	2.0 mm	2.5 mm	3.0 mm	4.0 mm
180 MeV	0.54	1.0	1.6	2.3	4.2
450 MeV	3.2	5.4	8.3	12.1	19.5
883 MeV	9.9	17.7	25.7	33.1	44.4
1557 MeV	16.0	27.0	37.8	49.0	66.5

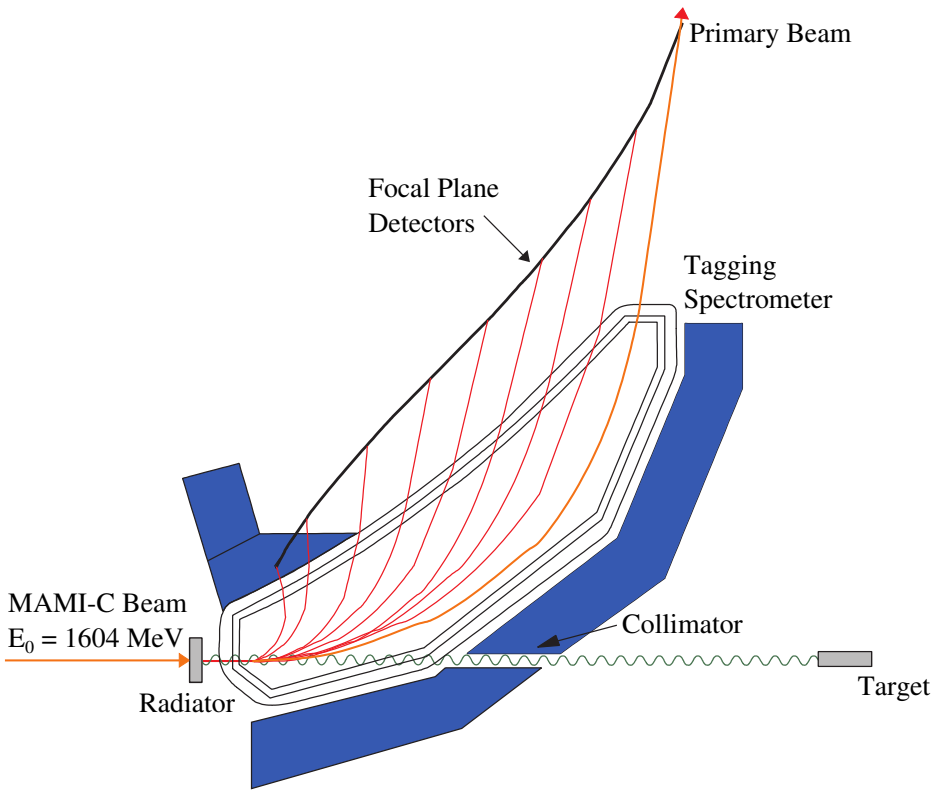

Figure 11: The Glasgow-Mainz photon tagging spectrometer.

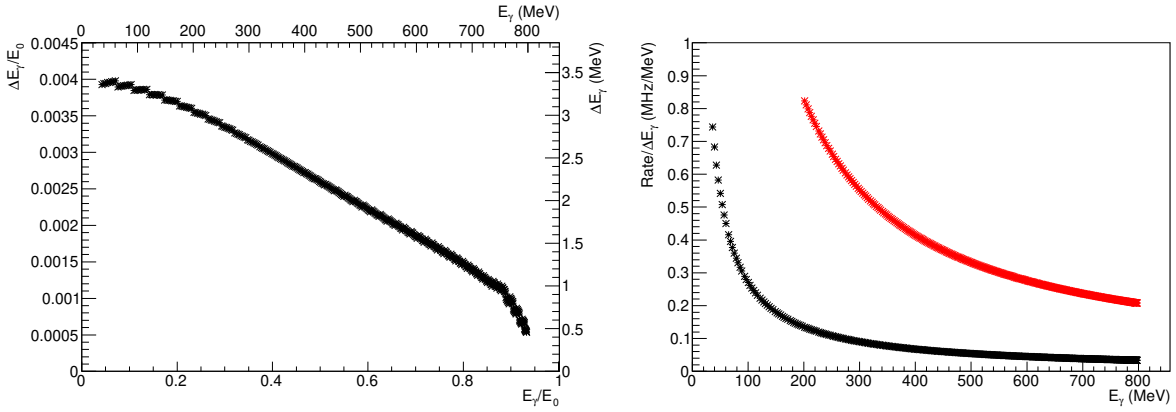

(a) Tagger resolution

(b) Tagger rate

Figure 12: (a) Tagger channel width (resolution) as a function of the tagged photon energy. The left and bottom axes show these values as relative to the incoming electron beam energy. The right and top axes show these values for a standard electron beam energy of 855 MeV. (b) Rates in MHz per MeV for a beam energy of 855 MeV, assuming a $1/E_\gamma$ Bremsstrahlung distribution, if the first channel is run at 2.5 MHz (black) or if the first 48 channels are switched off and the next is run at 2.5 MHz (red).

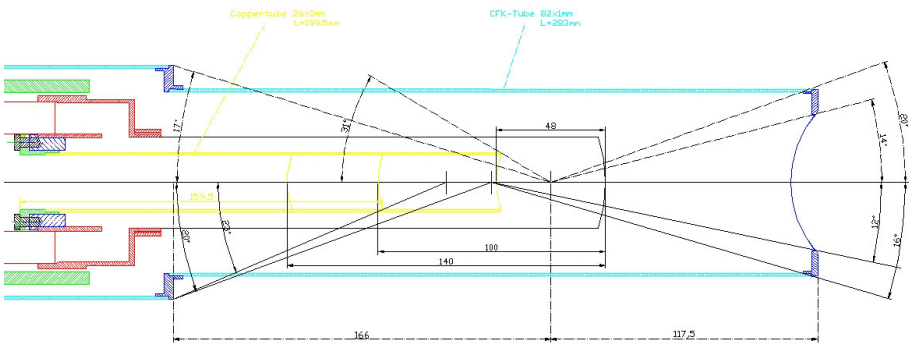

Figure 13: The A2 hydrogen target geometry and acceptance is shown for cell length of 48mm and 100mm.

B The liquid Hydrogen (Deuterium) target

The Hydrogen (Deuterium) target apparatus uses a cold head to liquefy the target gas from a 2 m^3 storage container into a cylindrical, thin walled plastic cell at temperatures around $\approx$ 20 K ($\approx$ 24 K). The pressure of the saturated target liquid is stabilized by a dedicated control system to typically 1080 ± 2 mBar for both isotopes. This leads to a density of $(70.548 \pm 0.01) \cdot 10^{-3}$ g/cm^3 for Hydrogen ($(163.24 \pm 0.02) \cdot 10^{-3}$ g/cm^3 for Deuterium). The Hydrogen target was designed to retain the high angular acceptance of the detector system. The acceptance of the hydrogen target is shown in Fig. 13. This system provides a low material budget in the region between 21° and 159° in the polar angle (θ) and over the full azimuthal (ϕ) range, adapted to our central detector Crystal Ball. At forward angles, less than 21°, were reaction products are detected in the TAPS forward wall, a thin ($\approx$ 2.5 mm) aluminium flange is used with a glued on 125 μm thick Kapton window.

The target length can be changed by using different entrance window adapters to 30.2 ± 0.3 mm, 47.2 ± 0.5 mm or 100.0 ± 1.0 mm. The cell for the target liquid is made of 125 μm Kapton, surrounded by 8 layers superisolation foil (each 8 μm Mylar + 2 μm Aluminum). A Carbon fibre tube of 82 mm outer diameter and 1 mm wall thickness holds the isolation vacuum.

B.1 Crystal Ball Detector System

The central detector system consists of the Crystal Ball calorimeter combined with a barrel of scintillation counters for particle identification and two coaxial multiwire proportional counters for charged particle tracking. This central system provides position, energy and timing information for both charged and neutral particles in the region between 21° and 159° in the polar angle (θ) and over almost the full azimuthal (ϕ) range. At forward angles, less than 21°, reaction products are detected in the TAPS forward wall. The full, almost hermetic, detector system is shown schematically in Fig. 14 and the measured two-photon invariant mass spectrum is shown in Fig. 15.

The Crystal Ball detector (CB) is a highly segmented 672-element NaI(Tl), self triggering photon spectrometer constructed at SLAC in the 1970's. Each element is a truncated triangular pyramid, 41 cm (15.7 radiation lengths) long. The Crystal Ball has an en-

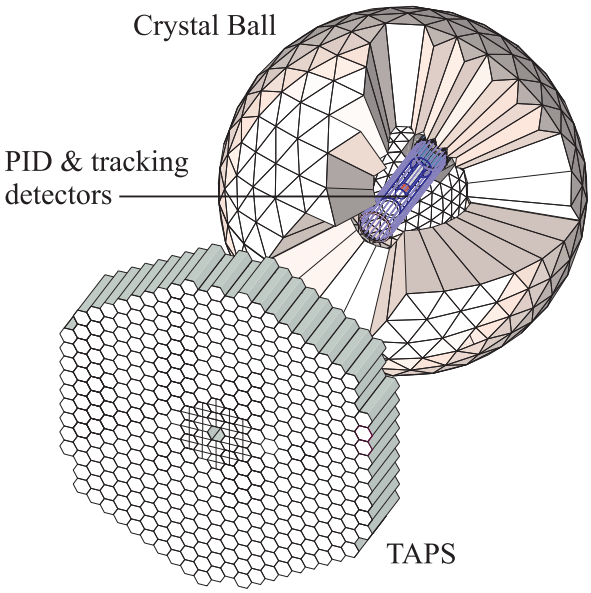

Figure 14: The A2 detector setup: The Crystal Ball calorimeter, with cut-away section showing the inner detectors, and the TAPS forward wall.

ergy resolution of $\Delta E/E = 0.020 \cdot E[\mathrm{GeV}]^{0.36}$, angular resolutions of $\sigma_\theta = 2 \ldots 3°$ and $\sigma_\phi = \sigma_\theta / \sin\theta$ for electromagnetic showers [29]. The readout electronics for the Crystal Ball were completely renewed in 2003, and it now is fully equipped with SADCs which allow for the full sampling of pulse-shape element by element. In normal operation, the onboard summing capacity of these ADCs is used to enable dynamic pedestal subtraction and the provision of pedestal, signal and tail values for each element event-by-event. Each CB element is also newly equipped with multi-hit CATCH TDCs. The readout of the CB is effected in such a way as to allow for flexible triggering algorithms. There is an analogue sum of all ADCs, allowing for a total energy trigger, and also an OR of groups of sixteen crystals to allow for a hit-multiplicity second-level trigger - ideal for use when searching for high multiplicity final states.

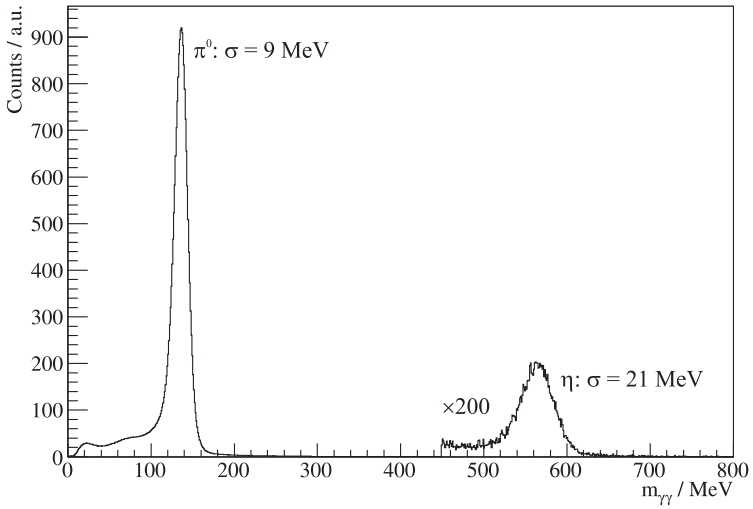

Figure 15: Two photon invariant mass spectrum for the CB/TAPS detector setup. Both η and π^0 mesons can be clearly seen.

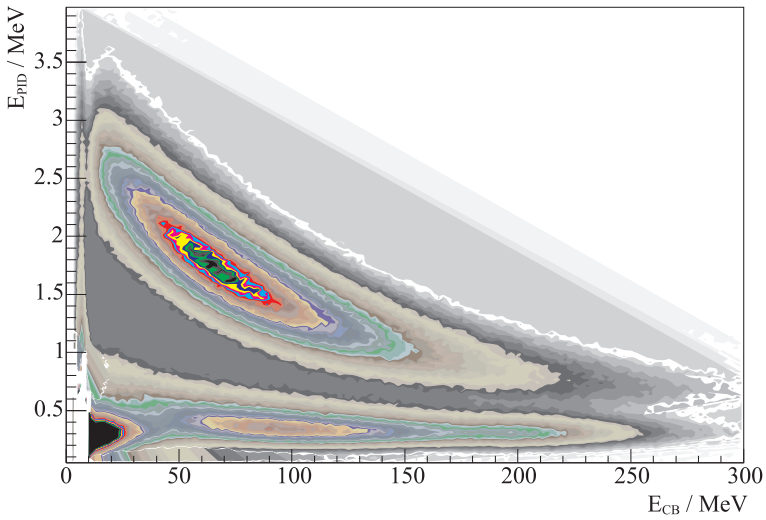

Figure 16: A typical $\Delta E/E$ plot from the Crystal Ball and the PID detector. The upper curved region is the proton locus, the lower region contains the pions and the peak towards the origin contains mostly electrons.

In order to distinguish between neutral and charged particles species detected by the Crystal Ball, the system is equipped with PID, a barrel detector of twenty-four 50 mm long, 4 mm thick scintillators, arranged so that each PID scintillator subtends an angle of 15° in ϕ. By matching a hit in the PID with a corresponding hit in the CB, it is possible to use the locus of the $\Delta E, E$ combination to identify the particle species (Fig. 16). This is primarily used for the separation of charged pions, electrons and protons. The PID covers from 15° to 159° in θ.

The excellent CB position resolution for photons stems from the fact that a given photon triggers several crystals and the energy-weighted mean of their positions locates the photon position to better than the crystal pitch. For charged particles which deposit their energy over only one or two crystals, this is not so precise. Here the tracks of charged particles emitted within the angular and momentum acceptance of the CB detector will be reconstructed from the coordinates of point of intersections of the tracks with two coaxial cylindrical multiwire proportional chambers (MWPCs) with cathode strip readout. These MWPCs are similar to those installed inside the CB during the first round of MAMI-B runs [30]. The most significant difference is that all detector signals are taken at the upstream end of the MWPCs, minimising the material required and facilitating particle detection in the forward polar region.

A mixture of argon (79.5%), ethane (30%) and freon-CF_4 (0.5%) is used as the filling gas. This mixture is a compromise between charge multiplication and localization requirements imposed by the ionizing particle tracks.

Within each chamber both the azimuthal and the longitudinal coordinates of the avalanche will be evaluated from the centroid of the charge distribution induced on the cathode strips. The location of the hit wires(s) will be used to resolve ambiguities which arise from the fact that each pair of inner and outer strip cross each other twice. The expected angular resolution (rms) will be ∼2° in the polar emission angle θ and ∼3° in the azimuthal emission angle ϕ.

B.2 TAPS Forward Wall

The TAPS forward wall is composed of 384 BaF_2 elements, each 25 cm in length (12 radiation lengths) and hexagonal in cross section, with a diameter of 59 mm. The front of every TAPS element is covered by a 5 mm thick plastic veto scintillator. The single counter time resolution is $\sigma_t = 0.2$ ns, the energy resolution can be described by $\Delta E/E = 0.018 + 0.008/E[\mathrm{GeV}]^{0.5}$ [29]. The angular resolution in the polar angle is better than 1°, and in the azimuthal angle it improves with increasing θ, being always better than $1/R$ radian, where R is the distance in centimeters from the central point of the TAPS wall surface to the point on the surface where the particle trajectory meets the detector. The TAPS readout was custom built for the beginning of the CB@MAMI program and is effected in such a way as to allow particle identification by Pulse Shape Analysis (PSA), Time Of Flight (TOF) and $\Delta E/E$ methods (using the energy deposit in the plastic scintillator to give ΔE). TAPS can also contribute to the CB multiplicity trigger and is currrently divided into upto six sectors for this purpose. The 2 inner rings of 18 BaF_2 elements have been replaced recently by 72 $PbWO_4$ crystals each 20 cm in length (22 radiation lengths). The higher granularity improves the rate capability as well as the angular resolution. The crystals are operated at room temperature. The energy resolution for photons is similar to BaF_2 under these conditions [31].

References

[1] L. G. Landsberg. Electromagnetic Decays of Light Mesons. *Phys. Rept.*, 128:301–376, 1985.

[2] J. J. Sakurai. Theory of strong interactions. *Annals Phys.*, 11:1–48, 1960.

[3] C. Terschlsen, S. Leupold, and M. F. M. Lutz. Electromagnetic Transitions in an Effective Chiral Lagrangian with the η' and Light Vector Mesons. *Eur. Phys. J.*, A48:190, 2012.

[4] S. P. Schneider, B. Kubis, and F. Niecknig. The $\omega \to \pi^0\gamma^*$ and $\phi \to \pi^0\gamma^*$ transition form factors in dispersion theory. *Phys. Rev.*, D86:054013, 2012.

[5] F. Niecknig, B. Kubis, and S. P. Schneider. Dispersive analysis of $\omega \to 3\pi$ and $\phi \to 3\pi$ decays. *Eur. Phys. J.*, C72:2014, 2012.

[6] I. V. Danilkin, C. Fernndez-Ramrez, P. Guo, V. Mathieu, D. Schott, M. Shi, and A. P. Szczepaniak. Dispersive analysis of $\omega/\phi \to 3\pi, \pi\gamma^*$. *Phys. Rev.*, D91(9):094029, 2015.

[7] R Arnaldi et al. Evidence for the production of thermal-like muon pairs with masses above 1 GeV/c^2 in 158A GeV Indium-Indium Collisions. *Eur. Phys. J.*, C59:607–623, 2009.

[8] B. Ananthanarayan, Irinel Caprini, and Bastian Kubis. Constraints on the $\omega\pi$ form factor from analyticity and unitarity. *Int. J. Mod. Phys.*, 31(14n15):1630020, 2016.

[9] I. Caprini. Testing the consistency of the $\omega\pi$ transition form factor with unitarity and analyticity. *Phys. Rev.*, D92(1):014014, 2015.

[10] R. R. Akhmetshin et al. Study of the process $e^+e^- \to \omega\pi^0 \to \pi^0\pi^0\gamma$ in c.m. energy range 920 MeV-1380 MeV at CMD-2. *Phys. Lett.*, B562:173–181, 2003.

[11] R. I. Dzhelyadin et al. Study of the Electromagnetic Transition Form-factor in $\omega \to \pi^0\mu^+\mu^-$ Decay. *Phys. Lett.*, 102B:296, 1981. [JETP Lett.33,228(1981)].

[12] R. Arnaldi et al. Precision study of the $\eta \to \mu^+\mu^-\gamma$ and $\omega \to \mu^+\mu^-\pi^0$ electromagnetic transition form-factors and of the $\rho \to \mu^+\mu^-$ line shape in NA60. *Phys. Lett.*, B757:437–444, 2016.

[13] G. W. Bennett et al. Final Report of the Muon E821 Anomalous Magnetic Moment Measurement at BNL. *Phys. Rev. D*, 73:072003, 2006.

[14] A. Keshavarzi, D. Nomura, and T. Teubner. Muon $g-2$ and $\alpha(M_Z^2)$: a new data-based analysis. *Phys. Rev.*, D97(11):114025, 2018.

[15] B. Lee Roberts. The Fermilab muon (g-2) project. *Nucl. Phys. Proc. Suppl.*, 218:237–241, 2011.

[16] Hiromi Iinuma. New approach to the muon g-2 and EDM experiment at J-PARC. *J. Phys. Conf. Ser.*, 295:012032, 2011.

[17] I. Danilkin, C. F. Redmer, and M. Vanderhaeghen. The hadronic light-by-light contribution to the muon's anomalous magnetic moment. *Prog. Part. Nucl. Phys.*, 107:20–68, 2019.

[18] P. Adlarson et al. Measurement of the $\omega \to \pi^0 e^+ e^-$ and $\eta \to e^+ e^- \gamma$ Dalitz decays with the A2 setup at MAMI. *Phys. Rev.*, C95(3):035208, 2017.

[19] A. Neiser. *Prototype development for a new readout of the CB/A2 setup and Analysis of the relative branching fraction of the $\eta' \to \omega\gamma$ decay.* PhD thesis, Mainz U., 2018.

[20] R. Escribano, S. Gonzàlez-Solís, R. Jora, and E. Royo. A theoretical analysis of the doubly radiative rare decays $\eta^{(\prime)} \to \pi^0\gamma\gamma$ and $\eta' \to \eta\gamma\gamma$. 2018.

[21] I. Danilkin, O. Deineka, and M. Vanderhaeghen. Theoretical analysis of the $\gamma\gamma \to \pi^0\eta$ process. *Phys. Rev.*, D96(11):114018, 2017.

[22] B. M. K. Nefkens et al. New measurement of the rare decay $\eta \to \pi^0\gamma\gamma$ with the Crystal Ball/TAPS detectors at the Mainz Microtron. *Phys. Rev.*, C90(2):025206, 2014.

[23] L. Ametller, J. Bijnens, A. Bramon, and F. Cornet. Chiral perturbation theory for $\eta \to \pi^0\gamma\gamma$. *Phys. Lett.*, B276:185–190, 1992.

[24] S. Prakhov et al. High-statistics measurement of the $\eta \to 3\pi^0$ decay at the Mainz Microtron. *Phys. Rev. C*, 97(6):065203, 2018.

[25] G. Colangelo, S. Lanz, H. Leutwyler, and E. Passemar. Dispersive analysis of $\eta \to 3\pi$. *Eur. Phys. J. C*, 78(11):947, 2018.

[26] A. Anastasi et al. Precision measurement of the $\eta \to \pi^+\pi^-\pi^0$ Dalitz plot distribution with the KLOE detector. *JHEP*, 05:019, 2016.

[27] C. O. Gullstrom, A. Kupsc, and A. Rusetsky. Predictions for the cusp in $\eta \to 3\pi^0$ decay. *Phys. Rev. C*, 79:028201, 2009.

[28] J. C. McGeorge et al. Upgrade of the Glasgow photon tagging spectrometer for Mainz MAMI-C. *Eur. Phys. J.*, A37:129–137, 2008.

[29] S. Prakhov et al. Measurement of the Slope Parameter alpha for the $\eta \to 3\pi^0$ decay with the Crystal Ball at MAMI-C. *Phys. Rev.*, C79:035204, 2009.

[30] G. Audit et al. DAPHNE: A Large acceptance tracking detector for the study of photoreactions at intermediate-energies. *Nucl. Instrum. Meth.*, A301:473–481, 1991.

[31] R. Novotny, R. Beck, W. Doring, V. Hejny, M. Hoek, A. Hofstaetter, V. Metag, and K. Romer. Scintillators for photon detection at medium energies: A comparative study of BaF-2, CeF-3 and PbWO-4. *Nucl. Instrum. Meth.*, A486:131–135, 2002.